*metals*

MDPI

*Supplementary Material*

# In-Depth Understanding of Hardmetal Corrosion Performance Reveals a Path to the Electrochemical Demolition of Scrap

**Benedetto Bozzini [1,*], Francesco Tavola [1], Augusto Travella [1], Alessandro Alleva [1], Claudio Mele [2], Elisa Emanuele [1], Sandra Tedeschi [3] and Gian Pietro De Gaudenzi [3]**

[1] Dipartimento di Energia, Politecnico di Milano, Via Lambruschini 4, 20156 Milano, Italy; francesco.tavola@polimi.it (F.T.); augusto.travella@zsw-bw.de (A.T.); alessandro.alleva@polimi.it (A.A.); elisa.emanuele@polimi.it (E.E.)
[2] Dipartimento di Ingegneria dell'Innovazione, Università del Salento, Via Monteroni, 73100 Lecce, Italy; claudio.mele@unisalento.it
[3] F.I.L.M.S. S.p.A.—Gruppo O.M.C.D., Via Megolo, 49, 28877 Anzola d'Ossola (Verbania), Italy; mst.miscele@omcd.it (S.T.); mgd.miscele@omcd.it (G.P.D.G.)
* Correspondence: benedetto.bozzini@polimi.it

**Citation:** Bozzini, B.; Tavola, F.; Travella, A.; Alleva, A.; Mele, C.; Emanuele, E.; Tedeschi, S.; De Gaudenzi, G.P. In-Depth Understanding of Hardmetal Corrosion Performance Reveals a Path to the Electrochemical Demolition of Scrap. *Metals* **2023**, *13*, 1376. https://doi.org/10.3390/met13081376

Academic Editor(s): Haiming Ding

Received: 13 June 2023
Revised: 12 July 2023
Accepted: 17 July 2023
Published: 31 July 2023



## S1 Details on the sequential CV measurement method

The corrosion of HM grades is an inherently transient-state phenomenon, in which compositional variations, phase modification and phase formation processes take place simultaneously, leading to irreversible and cumulative chemical and structural variations.

In this context, it is not clear whether a steady state can be achieved at all, and, in case it is, what its physico-chemical meaning is. Moreover, corrosion studies of HM are generally based on traditional electrochemical methods—mainly linear-sweep voltammetry (LSV) and EIS—the results of which can be interpreted with great difficulty in the case of time-dependent material properties. Moreover, exhaustive analysis of the literature reporting LSV data reveals that, with the exception of [S1] where a quantitative analysis was proposed, in the totality of other cases, the discussion of the results is limited to a description of the qualitative features of the curves [S2-S10].

The scenario found in systematic CV measurements is significantly more complex than the one represented in the literature. In fact, during an LSV measurement, the HM composition changes dynamically, leading to differences in response to the scan rate. Moreover, if the LSV scan is reversed or if it is repeated, the HM state at the beginning of the reversal period or of the repeated scan is that resulting from the integral of all the conditions undergone in the previous test, typically encompassing active dissolution, pseudopassivation and transpassivity conditions. The application of these conditions in sequence causes profound and irreversible modifications of both the binder and the hard phase. Moreover, LSV measurements are typically preceded by a so-called equilibration period at OCP [S11] that, again, in principle, brings about changes in the surface state of the HM, depending on the aggressiveness of the electrolyte employed. In the case of the neutral sulfate electrolyte employed in the present investigation, the variation of the HM surface at OCP can be regarded to be negligible with respect to those brought about by applied anodic polarization. If this condition holds, EIS measurements at OCP are reasonably representative of the state of the HM attained before this particular test. Meanwhile, in the case of EIS tests with applied potential, the stationarity requirement is generally not met (for an in-depth discussion of methodological aspects of EIS of HM, see [S1]).

## S2 Model for linear-sweep voltammetry measurements of HM grades and fitting of experimental data

The classes of electrochemical behavior, defined and discussed in Section 3.1 of the main text, can be employed to form the basis of a general phenomenological model for

linear-sweep voltammetries, either measured directly or extracted from CV curves of HM grades, presented in Eq. (S1).

$$i(V) = [i_{o1} \cdot f_{BV}(V_1, B_1) + i_{P1}] \cdot \Sigma^{-}(V_a, \Delta_a) + [i_P + i_{o2} \cdot f_T(V_2, B_2) + i_{o3} \cdot f_T(V_3, B_3)] \cdot \Sigma^{+}(V_b, \Delta_b) \quad \text{(S1)}$$

Where $f_{BV}$ represents the Butler–Volmer equation, $f_T$ represents the Tafel equation, $\Sigma^-$ and $\Sigma^+$ are the sigmoidal equations and $i_P$ is the pseudopassivation current density (c.d.). Non-linear least-square fitting was performed with the Levenberg–Marquardt methods, implemented in the Origin software. The first term in the sum describes the low-overvoltage range, encompassing active corrosion for grade Co-Ni and the electrochemical behavior in the pseudopassive state brought about by environmental exposure for the remaining ones. The second term denotes, on the one hand, the pseudopassive range found with grade Co-Ni and, on the other hand, the primary and secondary transpassivity typical of Ni-Co, Co-Ni-Cr-Mo and Ni-Co-Cr-Mo at intermediate overvoltages. Finally, this term accounts for transpassive conditions. Two electrokinetic processes were found in the low-overvoltage range and up to three in the high-anodic range. The whole sets of anodic-going scans, extracted from CV curves obtained by varying the ATV for the four grades investigated, could be accurately fitted with some of the components of the general form of the model explained above. The non-linear least-square fits in the whole investigated potential range are shown, together with the measured data in Figure 2 and details on the implementation of Eq. (S1) for the individual grades are reported below.

*2.1. Fitting of the CVs of Figure 1a for grade Co-Ni with Eq. (S1)*

In the case of grade Co-Ni, Eq. (S1) is implemented in the forms of Eq.s (S1.1) and (S1.2) for ATV below and above the critical ATV of 640 $V_{Ag/AgCl}$, corresponding to one of the $E_{crit}$ values listed in Figure 2 of the main text.

$$\text{ATV} < 640\ \text{mV}_{Ag/AgCl} = \text{ATV}_{crit}$$

$$i(V) = [i_{o1} \cdot f_{BV}(V_1, B_1) + A \cdot V] \cdot \Sigma^{-}(V_a, \Delta_a) \quad \text{(S1.1)}$$

Eq. (S1.1)

$$\text{ATV} > 640\ \text{mV}_{Ag/AgCl}$$

$$i(V) = [i_{o1} \cdot f_{BV}(V_1, B_1) + i_{P1}] \cdot \Sigma^{-}(V_a, \Delta_a) + [i_P + i_{o2} \cdot f_T(V_2, B_2) + i_{o3} \cdot f_T(V_3, B_3)] \cdot \Sigma^{+}(V_b, \Delta_b) \quad \text{(S1.2)}$$

where $\Sigma^{-}(V_a,\Delta_a)$ denotes deactivation of function [•] and $\Sigma^{+}(V_b,\Delta_b)$ the activation of function [•].

The physico-chemical meaning of Eq. (S1.1) is that, at low-anodic overvoltages (below $ATV_{crit}$), grade Co-Ni undergoes active corrosion of the binder, that—owing to its multi-element composition—can be described by two electrokinetic processes. One of these is farther from equilibrium and is expressed by a full BV equation $i_{o1} \cdot f_{BV}(V_1,B_1)$, and the second one is closer to equilibrium and can be described by a linearized BV equation ($A \cdot V$). These processes lead to pseudopassivation, the development of which can be described by the Boltzmann equation with negative slope $\Sigma^{-}(V_a,\Delta_a)$ with inflection point at $V_a$ and width $\Delta_a$. After pseudopassivation, on the one hand, the behavior at low-anodic overvoltages is modified and, on the other hand, a second set of processes is activated (Eq. (S1.2), as expressed by the Boltzmann equation with positive slope $\Sigma^{+}(V_b,\Delta_b)$, with inflection point at $V_b$ and width $\Delta_b$). In the low-overvoltage range (quantified by $\Sigma^{-}(V_a,\Delta_a)$), only one electrokinetic process is required, in addition to a constant c.d. $i_{p1}$, positively corre-

lated with the ATV (Figure S6(b)), that can be interpreted with a pseudopassive c.d. resulting from previous polarization at ATV in excess of $ATV_{crit}$. In the high-overvoltage range (characterized by $\Sigma^{+}(V_b,\Delta_b)$), a pseudopassivity c.d. $i_P$ develops and transpassivity is attained in two steps, described by two Tafel equations $i_{o2}\cdot f_T(V_2,B_2)$ and $i_{o3}\cdot f_T(V_3,B_3)$.

*2.2. Fitting of the CVs of Figure 1a for grades Ni-Co, Co-Ni-Cr-Mo and Ni-Co-Cr-Mo with Eq. (S1)*

In the case of grades Ni-Co, Co-Ni-Cr-Mo and Ni-Co-Cr-Mo, Eq. (S1) is implemented in the forms of Eq.s (S1.3) and (S1.4) for ATV below and above the critical ATVs specified below, again corresponding $E_{crit}$ values selected from the list of Figure 2 of the main text.

$$\text{ATV} < \text{ATV}_{crit}$$
$$i(V) = i_{o1}\cdot f_{BV}(V_1,B_1) + A\cdot V \quad \text{(S1.3)}$$

$\text{ATV} > \text{ATV}_{crit}$, being: $\text{ATV}_{crit}$(Ni-Co)=830 $\text{mV}_{Ag/AgCl}$; $\text{ATV}_{crit}$(Co-Ni-Cr-Mo)= 840 $\text{mV}_{Ag/AgCl}$ and $\text{ATV}_{crit}$(Ni-Co-Cr-Mo)=845 $\text{mV}_{Ag/AgCl}$.

$$i(V) = i_{o1}\cdot f_{BV}(V_1,B_1) + A\cdot V + [i_P + i_{o2}\cdot f_{BV}(V_2,B_2) + i_{o3}\cdot f_{BV}(V_3,B_3)]\cdot \Sigma^{+}(V_b,\Delta_b) \quad \text{Eq. (S1.4)} \quad \text{(S1.4)}$$

Grades Ni-Co, Co-Ni-Cr-Mo and Ni-Co-Cr-Mo are pseudopassive under ambient conditions, and their behavior at low-anodic overvoltages (below $ATV_{crit}$) is described by low-rate pseudopassive corrosion (Eq. (S1.3)), again following two electrokinetic processes as in Eq. (S1.1). The transpassive behavior above $ATV_{crit}$ (Eq. (S1.4)) can be described in the same way as for grade Co-Ni (see comments on the second addend of Eq. (S1.2)).

The fit parameters for Eq.s (S1.1)–(S1.4) are reported in Table S1 and in Panels (c–f) of Figure S6.

Parameter $i_{o1}$ (Figure S6(c)), the effective exchange c.d. in the low-anodic overvoltage range where binder corrosion is the dominating process, correlates with the corrosion resistance ranking Co-Ni<Ni-Co<Co-Ni-Cr-Mo<Ni-Co-Cr-Mo, for Co-Ni grows with ATV, denoting progressive denobling of the binder phase, and decreases in the OER range, probably owing to incipient mechanical damage of the corrosion product layer, as highlighted in Section 3.3 of the main text.

Also, parameter $V_1$ (Figure S6(d))—the effective activation voltage of the key corrosion process at low-anodic voltages—correlates with the corrosion resistance ranking of the grades and, in the case of the Cr-Mo-containing systems, it exhibits a progressive growth with ATV, denoting progressive inhibition of the corrosion process involving the binder.

With the exception of grade Ni-Co-Cr-Mo, the values of the effective anodic Tafel slope in the low-anodic overvoltage range $B_1$ (Figure S6(e)) are typically higher than expected for classical mechanisms with electrochemical and chemical steps [S12]. This denotes the presence of layers inhibiting charge transfer, as expected in systems undergoing pseudopassivation. In the low-overvoltage range, $B_1$ values anticorrelate with the corrosion resistance ranking of the materials, while higher values are found when the ATV reaches the transpassive range, where $B_1$ tends to grow, becoming similar for all grades, apart from Ni-Co-Cr-Mo. This can be explained with the fact that extensive corrosion of WC in the transpassive range leads to progressive inhibition of binder corrosion. This phenomenon correlates with the formation of W- and Co-containing mixed oxides [S13, S14]. The $B_1$ values for the highly corrosion-resistant grade Ni-Co-Cr-Mo, that are low and independent of the ATV, indicate that the corrosion mechanism in the binder range is stable and controlled by the synergy of Ni and Cr+Mo.

*A* is required only for grades w/o Cr+Mo (Co-Ni and Ni-Co) and is higher for the higher-Co (less corrosion resistant) grade Co-Ni.

The model parameter $V_b$, denoting the onset of transpassivity (grade Co-Ni) or secondary transpassivity (other grades), was found to be close to $ATV_{crit}$, coherently with the definition of this quantity referring to a change in morphology of the CV curves (detailed in Section 3.1 of the main text). $V_b$ is lower for Co-Ni that is Co-rich w/o Cr-Mo and very similar for other, notably more corrosion-resistant, grades.

The pseudopassivity c.d. $i_p$ (Figure S6(f)) is about constant with respect to ATV for grades Co-Ni, Co-Ni-Cr-Mo and Ni-Co-Cr-Mo and anticorrelates clearly with the corrosion resistance of the grades. Grade Ni-Co, with a Ni-rich binder and no Cr+Mo additions, grows with the ATV, changing from relatively very low values to values intermediate between the level of grade Co-Ni and that of the grades with Cr+Mo. This shows that the binder with a high Ni/Co ratio is very effective in protecting the binder in the potential region in which WC is not severely attacked, while Cr+Mo additions synergize with the high-Ni binder to afford the stabilization of the corrosion resistance when the material is polarized in the transpassive range.

Regarding the model parameters for the transpassive range, the effective exchange c.d. values $i_{o2}$ and $i_{o3}$ and the effective Tafel slopes $B_2$ and $B_3$ essentially correlate with the corrosion resistance ranking, showing that the binder composition influences the corrosion mechanism in the WC corrosion range. Quantitatively, the largest difference is between grade Co-Ni and the other ones, showing that Ni and Cr have a larger impact in controlling transpassive corrosion, in keeping with literature reports on the effect of these alloying elements on corrosion resistance [S15, S16]. Coherently, the parameters $V_2$ and $V_3$, expressing the effective free-corrosion potentials for the transpassive charge-transfer processes, group around similar values, controlled by the conditions for the attack of WC, and essentially rank according to the corrosion resistance of the grades.

The values of the widths of the activation ($\Delta_a$) and deactivation ($\Delta_b$) Boltzmann functions all lie in the range ca. 30÷60 mV and do not exhibit a clearcut dependence on the specific grade.

**S3 OCP relaxation after potentiostatic tests**

To complement and deepen the potentiostatic tests described in Section 3.2.1 of the main text, we also measured the potential relaxation at OCP (Figure S7(a)) and EIS (Figure S7(b)) after attainment of OCP conditions. At all potentials and for all grades, a denobling transient was measured, after which the potential tends towards an asymptotic level, with the only exception of the fully developed transpassive conditions of grade Co-Ni, which initially shows transient ennobling before the denobling relaxation. The denobling transients can be explained with the relaxation of the concentration of diffusible corrosion products at the interface of an active electrode. The initial ennobling is instead due to a more complex interfacial compositional and structural relaxation of the more active grade Co-Ni. Consequently, the asymptotic OCP values are different (either more or less noble) from those of the pristine condition, depending on the binder composition and applied potential. OCP values correlate well with the subsurface composition in the low μm range, as measured by EDS (Figure 3(c) of the main text). It is worth noting that the presence of Cr+Mo tends to keep the OCP after corrosion closer to that found under pristine conditions, with a tendency to ennoble at potentials lower that the fully developed transpassive range.

Complementary insight into the corrosion processes taking place at the $E_{crit}$ values (Section 3.2 of the main text) is achieved by EIS spectra measured at OCP in the pristine state and after potentiostatic polarization (Figure S7(b)). The EIS fitting model is described in Section 3.2.2 of the main text and the fitting results are reported in Table 3, again in the main text. Grade Co-Ni shows evident activation after the PS tests. This activation is progressive under active corrosion conditions (240 mV), while the faradaic resistance grows progressively in the pseudopassive (340, 440 mV) and incipient transpassive (640 mV)

states. Grade Ni-Co exhibits passive behavior both at OCP and upon incipient secondary transpassivity (830 mV), with a slightly larger $R_F$ in the latter case. Grade Co-Ni-Cr-Mo, containing Cr+Mo, on the one hand shows much higher $R_F$ values with respect to Cr-free grades Co-Ni and Ni-Co and, on the other hand, a progressive activation with increasing anodic polarization. Instead, Ni-rich and Cr+Mo-containing grade Ni-Co-Cr-Mo exhibits high $R_F$—accompanied by mass-transport control at low frequency—together with a tendency to stronger passivation at higher anodic potentials, coherently with the ennobling observed in Figure S7(a). This unique behavior among the investigated HMs correlates straightforwardly with the high-Ni, Cr+Mo-containing binder composition.

**S4 Detailed analysis of the electrochemical HM demolition process**

As expounded in Section 3.3 and schematized in Figure 6 of the main text, electrochemical demolition of HMs can be obtained by the application of appropriate potentiostatic square-wave cycles, causing, sequentially: (a) the formation of corrosion product film, (b) release of $O_2$ bubbles at the film/metal interface, (c) film detachment. Figure S12 reports the c.d. response of the four investigated HM grades. It can be noticed that the apparent decrease in c.d., more evident in Figure S12(a, d), is a result of the reduction in active area of the sample, due to macroscopic shape changes resulting from the progress of demolition. Apart from these details, the c.d. levels found in the pulsed-corrosion experiments match closely with the values found in the potentiostatic staircase experiments of Figure S11.

Regarding the impact of pulsed corrosion on HM demolition, on the one hand, detachment of corrosion product disks is obtained with all grades but, on the other hand, some aspects of the process are material dependent. Specifically, with Co-Ni, the moment of detachment of the corrosion product disks very reproducibly occurs ca. 50 s after switching to OER conditions, and it is marked by a clear electrochemical signature: just before detachment, a dip in the current can be noticed (Figure S13(a)). This can be explained with the filling of the pores by gas, corresponding to a pressure build-up at the interface between the corrosion product film and the embedded electrochemically active interface that leads to film detachment.

A similar, though less reproducible, behavior is found with grade Ni-Co-Cr-Mo: here, the detachment occurs at each pulsed-corrosion cycle, ca. 150-500 s after having switched to OER conditions; the same electrochemical signature was found as with grade Co-Ni (Figure S13(b)). However, under the investigated conditions, disk detachment from samples Ni-Co and Co-Ni-Cr-Mo does not show a clear periodic behavior and it does not seem to correspond to each pulsed-corrosion cycle.

Despite the disk detachment grade dependence, all the low-potential corrosion steps show an essentially constant c.d. over time. In fact, the high-potential demolition step restores the surface available for the corrosion process, allowing the maintenance of a highly effective corrosion rate. This is further proved in Figure S14, which compares potentiostatic switching experiments with PS ones, carried out at the low-anodic polarization. In all cases, potential switching leads to higher anodic c.d., denoting effective activation; this effect is more marked for Co-rich grades (Co-Ni and Co-Ni-Cr-Mo), for which pseudopassivation is a state that can be reached with electrochemical control, as pinpointed in Section 3.2 of the main text.

**References**

[S1] B. Bozzini, B. Busson, G.P. De Gaudenzi, C. Humbert, C. Mele, S. Tedeschi, A. Tadjeddine, Corrosion of cemented carbide grades in petrochemical slurries. Part I - Electrochemical adsorption of $CN^-$, $SCN^-$ and MBT: A study based on in situ SFG, Int. J. of Refract. Met. and Hard Mater. 60 (2016) 37-51. https://doi.org/10.1016/j.ijrmhm.2016.06.010

[S2] L. Zhang, Y. Chen, Q.-L. Wan, T. Liu, J.-F Zhu, W. Tian, Electrochemical corrosion behaviors of straight WC–Co alloys: Exclusive variation in grain sizes and aggressive media, International Int. J. Refract. Hard Met 57 (2016) 70-77. https://doi.org/10.1016/j.ijrmhm.2016.02.009

[S3] B. Bozzini, A. Gianoncelli, G. Kourousias, M. Boniardi, Andrea C., Simone D. Zilio, R. Hussain, M. Kazemian Abyaneh, M. Kiskinova, C. Mele, S. Tedeschi, G.P. De Gaudenzi,The role of chromium in the corrosion performance of cobalt- and cobalt-nickel based hardmetal binders: A study centred on X-ray absorption microspectroscopy, Int. J. of Refract. Met. and Hard Mater. 92 (2020) 105320. https://doi.org/10.1016/j.ijrmhm.2020.105320

[S4] P.K. Katiyar, N.S. Randhawa, J.Hait, R.K. Jana, K.K. Singh, ,T.R. Mankhand, Anodic dissolution behaviour of tungsten carbide scraps in ammoniacal media. In Adv. Mat. Res., 828 (2014) 11–20. https://doi.org/10.4028/www.scientific.net/AMR.828.11

[S5] J.C. Lin, J.Y. Lin, S.P. Jou, Selective dissolution of the cobalt binder from scraps of cemented tungsten carbide in acids containing additives, Hydromet. 43 (1996) 47-61. https://doi.org/10.1016/0304-386X(96)00023-0

[S6] Q. Zhang, X. Xi, L. Zhang, M. Feng, Z. Nie, L. Ma, The electrochemical dissolution mechanism and treatment process in the molten-salt electrolytic recovery of WC-Co two-phase scraps, J. Electroanal. Chem. 896 (2021) 115219. https://doi.org/10.1016/j.jelechem.2021.115219

[S7] Y.F. Zheng, G. Fargas, E. Armelin, O. Lavigne, L. Llanes, Corrosion-Induced Damage and Residual Strength of WC-Co,Ni Cemented Carbides: Influence of Microstructure and Corrosion Medium, Metals 9 (2019) 1018. http://dx.doi.org/10.3390/met9091018

[S8] T. Oishi, M. Yaguchi, Influence of partial pressure of water vapor on anodic dissolution of tungsten from super hard alloy tools in molten sodium hydroxide, Int. J. of Refract. Met. and Hard Mater, 69 (2017) 254-258. https://doi.org/10.1016/j.ijrmhm.2017.08.018

[S9] W. Qiu, Y. Liu, J. Ye, H. Fan, Y. Qiu, Effects of (Ti,Ta,Nb,W)(C,N) on the microstructure, mechanical properties and corrosion behaviors of WC-Co cemented carbides, Ceram. Int., 43 (2017) 2918-2926. https://doi.org/10.1016/j.ceramint.2016.09.124

[S10] X. Zhang, J. Zhou, C. Liu, K. Li, W. Shen, Z. Lin, Z. Li, Y. He, N. Lin, Effects of Ni addition on mechanical properties and corrosion behaviors of coarse-grained WC-10(Co, Ni) cemented carbides, Int. J. Refract. Hard Met. 80 (2019) 123-129. https://doi.org/10.1016/j.ijrmhm.2019.01.004

[S11] A.M. Ferro Rocha, A.C. Bastos, J.P. Cardoso, F. Rodrigues, C.M. Fernandes, E. Soares, J. Sacramento, A.M.R. Senos, M.G.S. Ferreira, Behaviour of WC hardmetals with nickel-based binders, Corr. Sci. 147 (2019) 384-393. https://doi.org/10.1016/j.corsci.2018.11.015

[S12] A.R. Despić, Deposition and Dissolution of Metals and Alloys, Part B. In B.E. Conway, J.O'M. Bockris, E. Yeager, S.U.M. Khan, R.E. White, Comprehensive Treatise of Electochemistry, vol. 7, Plenum Press, N.Y. (1983) 466-480. https://doi.org/10.1007/978-1-4613-3584-9_8

[S13] Y.F. Zheng, G. Fargas, O. Lavigne, E. Roitero, L. Llanes, Corrosion-induced changes on Hertzian contact damage in cemented carbides, Int. J. Refract. Met. Hard Mater. 92 (2020) 105334. https://doi.org/10.1016/j.ijrmhm.2020.105334

[S14] G.P. De Gaudenzi, M. Amati, A. Gianoncelli, L. Gregoratti, M. Kiskinova, G. Kourousias, S. Tedeschi, B. Bozzini, The spatial organization of corrosion products at the hardmetal/environment interface, Proc. 20th Plansee Seminar, Reutte (A) 30/05÷03/06/2022, eds. Karlheinz Wex, Heinrich Kestler and Andreas Pilz, Plansee Group Functions Austria GmbH, Reutte/Tyrol, Austria.

[S15] R. Steinlechner, R. de Oro Calderon, T. Koch, P. Linhardt, W.D. Schubert, A study on WC-Ni cemented carbides: Constitution, alloy compositions and properties, including corrosion behaviour, Int. J. of Refract. Met. and Hard Mater. 103 (2022) 105750. https://doi.org/10.1016/j.ijrmhm.2021.105750

[S16] R.F. Santos, A.M. Ferro Rocha, A.C. Bastos, J.P. Cardoso, F. Rodrigues, C.M. Fernandes, J. Sacramento, M.G.S. Ferreira, A.M.R. Senos, C. Fonseca, M.F. Vieira, L.F. Malheiros, The effect of Cr content on the corrosion resistance of WC-Ni-Cr-Mo composites, Int. J. Refract. Met. Hard Mater. 95 (2021) 105434. https://doi.org/10.1016/j.ijrmhm.2020.105434

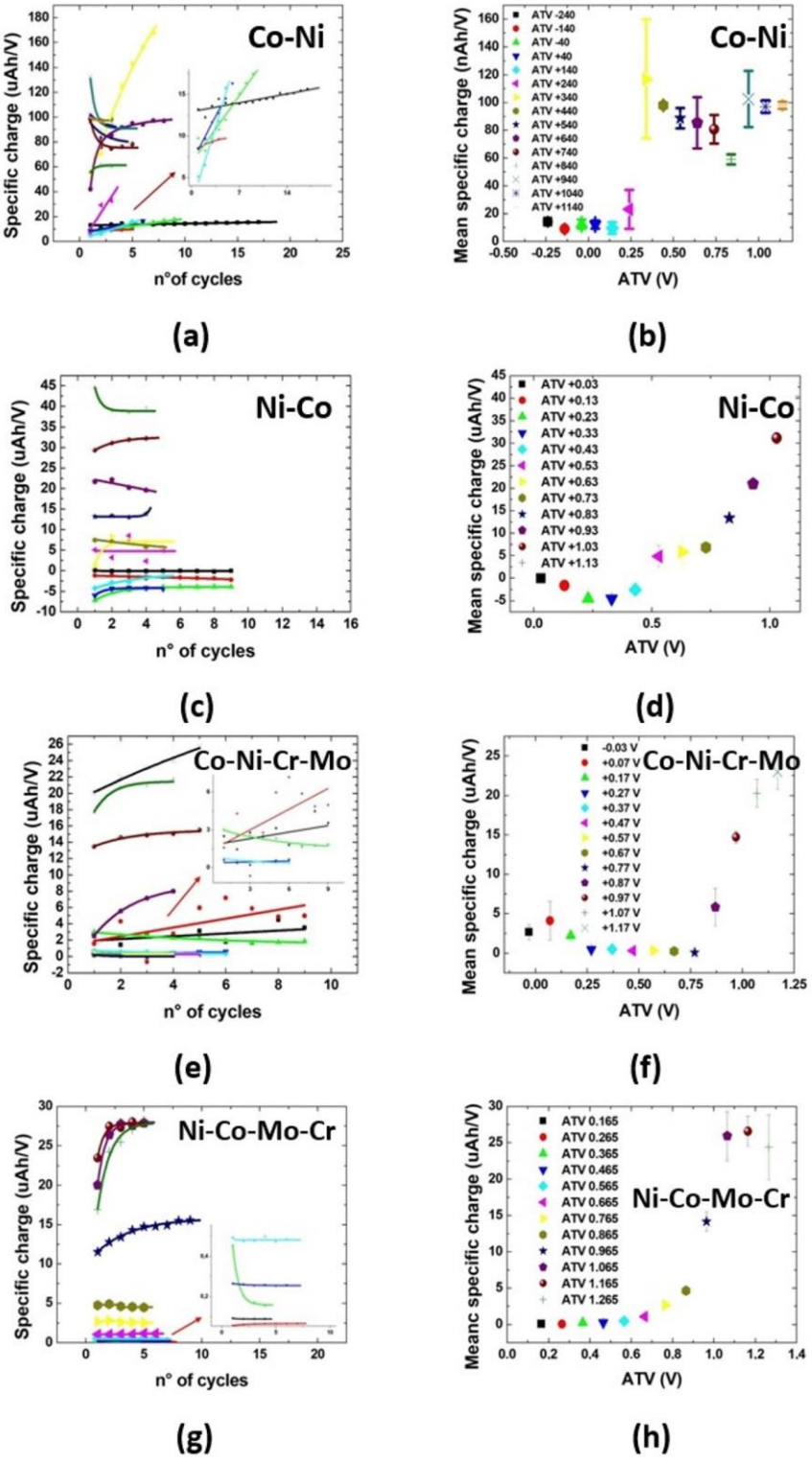


**Figure S1.** Quantitative analyses of the CVs of Figure 1(a–d) for the grades indicated in the panels. (a, c, e, g) Specific charge per cycle (rationed over the voltage span of a given CV), as a function of the number of cycles, for a given anodic terminal voltage (ATV, color-coded as shown in the image). (b, d, f, h) Specific charge per cycle vs. ATV, averaged over all cycles measured with a given ATV (an extract of these data is reported in Figure 1(f)). For ease of reference, the ATVs are color-coded in each panel. (a) Co-Ni , (b) Ni-Co, (c) Co-Ni-Cr-Mo, (d) Ni-Co-Cr-Mo.

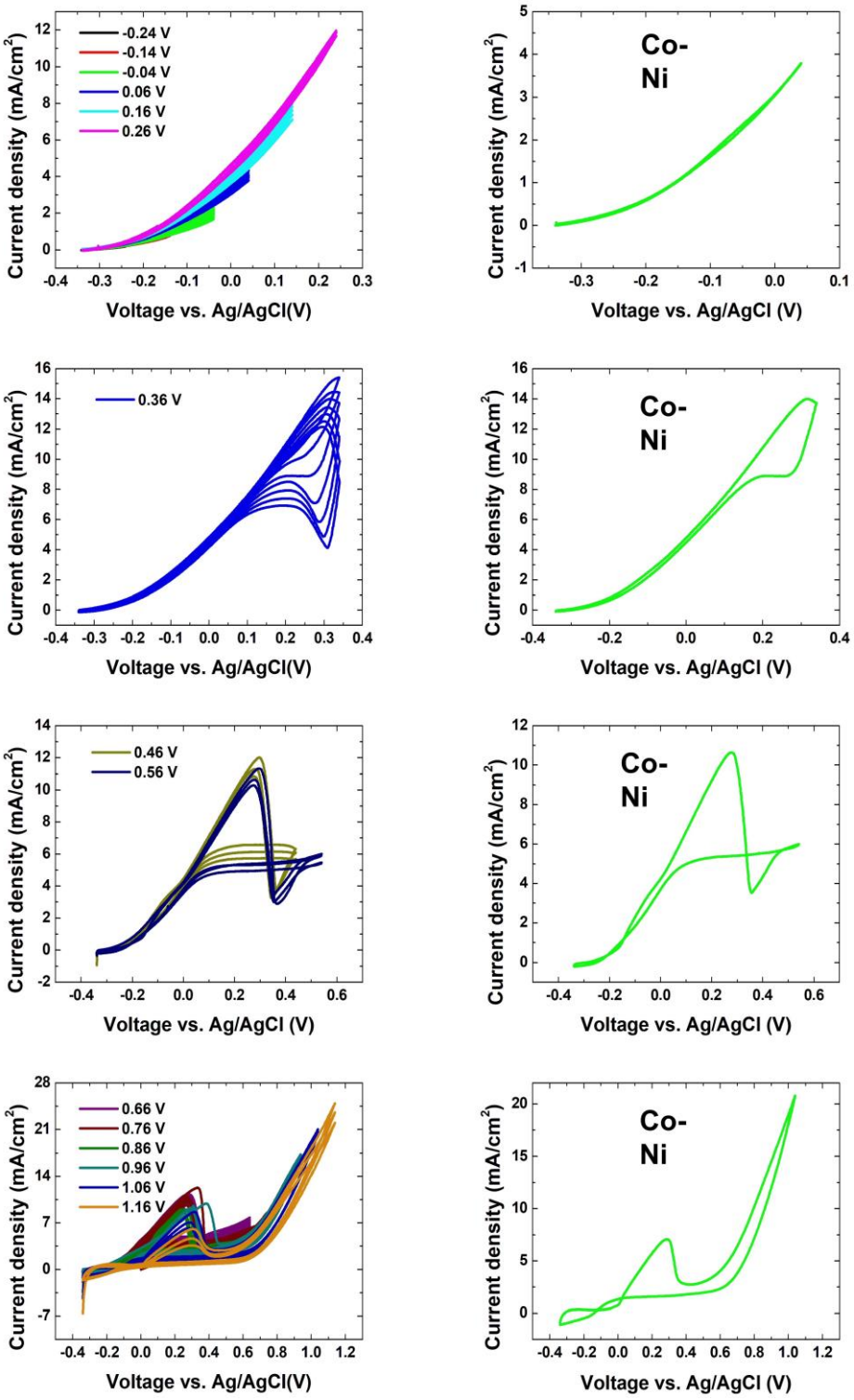


**Figure S2.** Grouping in classes of voltammetric shapes for the CVs measured by progressively shifting the anodic terminal voltage (ATV) with grade Co-Ni.

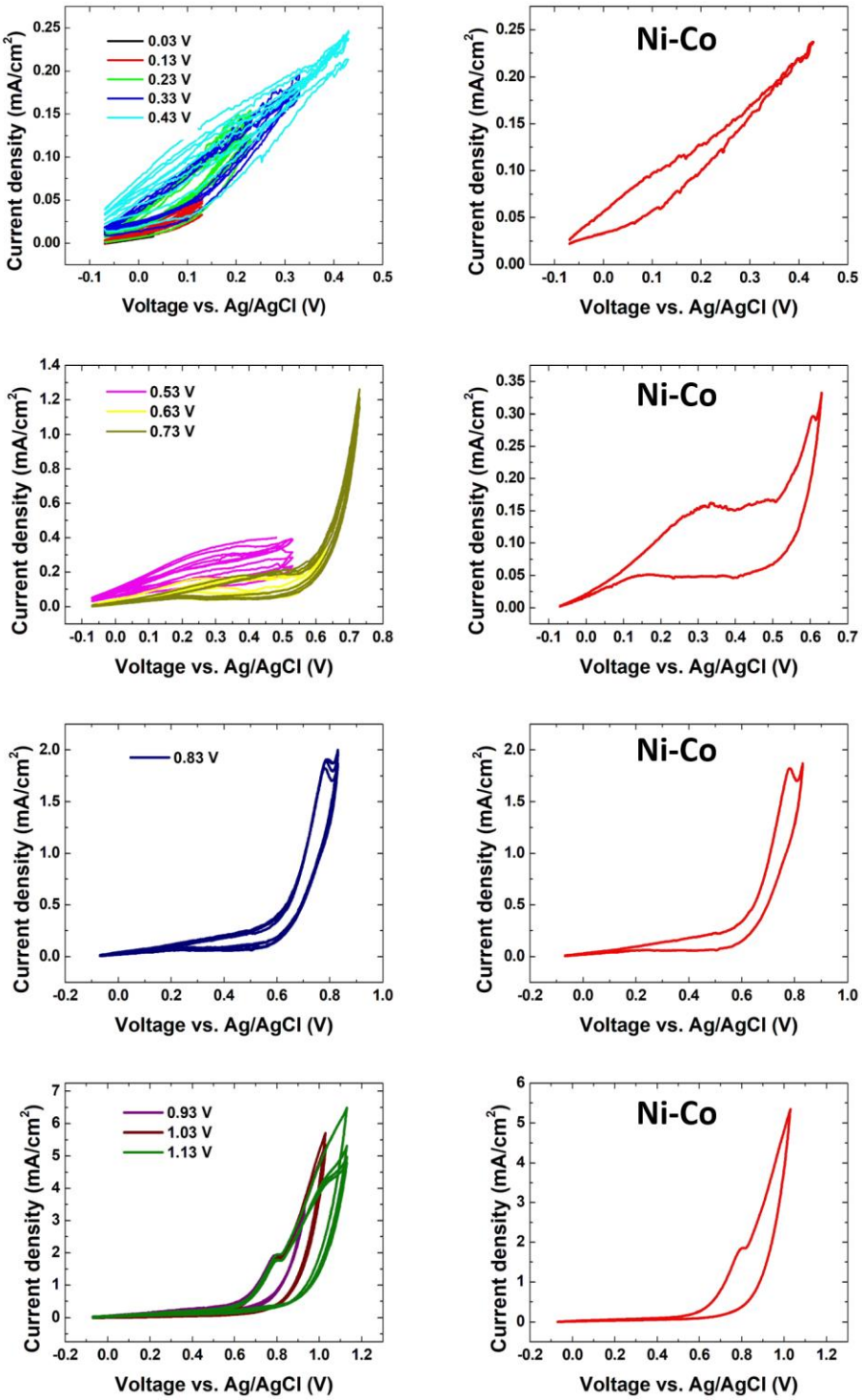


**Figure S3.** Grouping in classes of voltammetric shapes for the CVs measured by progressively shifting the anodic terminal voltage (ATV) with grade Ni-Co.

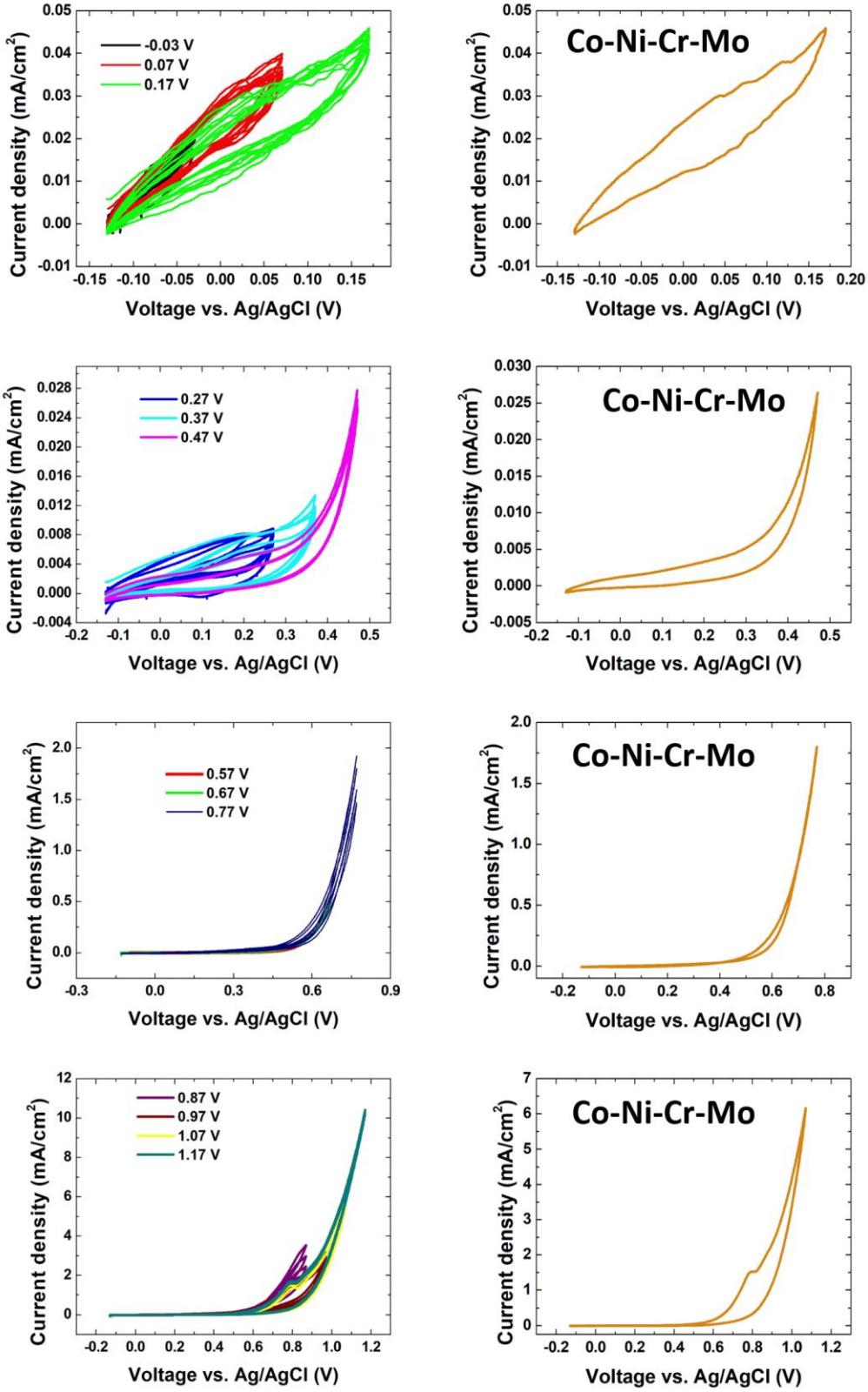


**Figure S4.** Grouping in classes of voltammetric shapes for the CVs measured by progressively shifting the anodic terminal voltage (ATV) with grade Co-Ni-Cr-Mo.

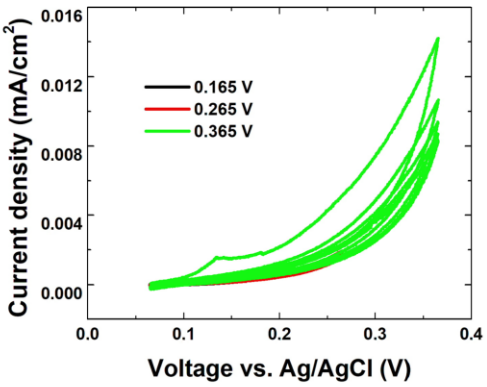
0.165 V
0.265 V
0.365 V
Current density (mA/cm²)
Voltage vs. Ag/AgCl (V)

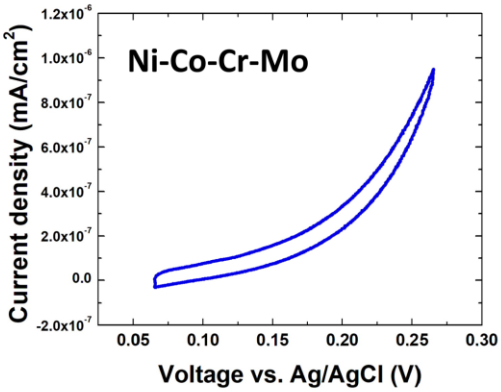
Ni-Co-Cr-Mo
Current density (mA/cm²)
Voltage vs. Ag/AgCl (V)

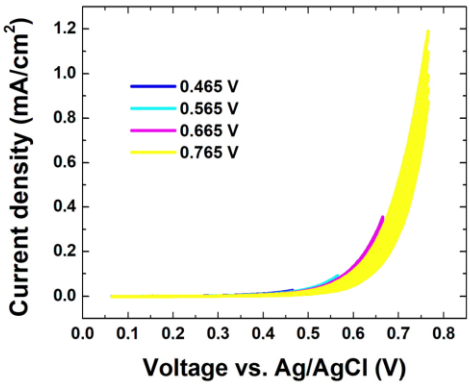
0.465 V
0.565 V
0.665 V
0.765 V
Current density (mA/cm²)
Voltage vs. Ag/AgCl (V)

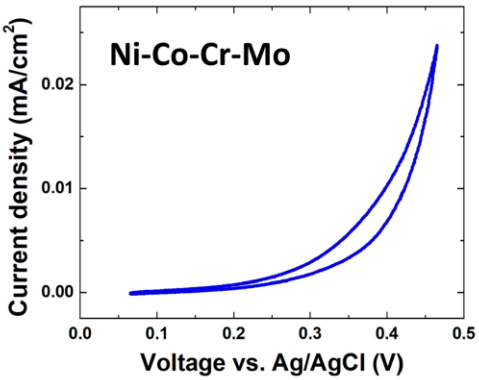
Ni-Co-Cr-Mo
Current density (mA/cm²)
Voltage vs. Ag/AgCl (V)

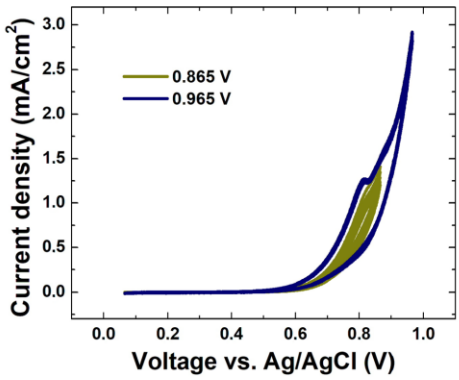
0.865 V
0.965 V
Current density (mA/cm²)
Voltage vs. Ag/AgCl (V)

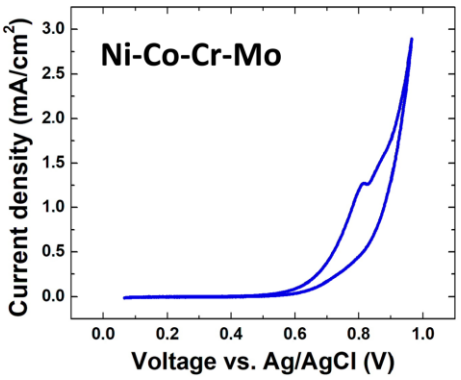
Ni-Co-Cr-Mo
Current density (mA/cm²)
Voltage vs. Ag/AgCl (V)

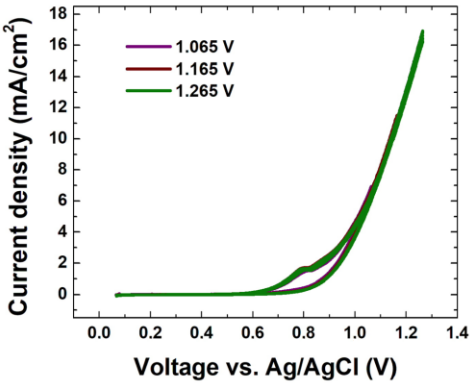
1.065 V
1.165 V
1.265 V
Current density (mA/cm²)
Voltage vs. Ag/AgCl (V)

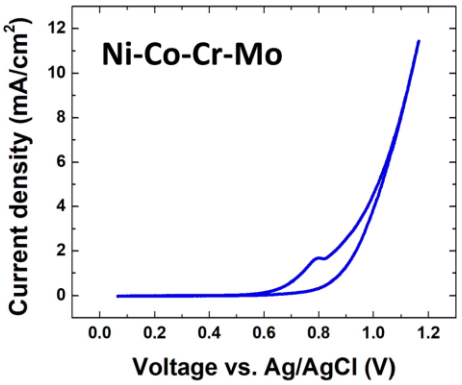
Ni-Co-Cr-Mo
Current density (mA/cm²)
Voltage vs. Ag/AgCl (V)

**Figure S5.** Grouping in classes of voltammetric shapes for the CVs measured by progressively shifting the anodic terminal voltage (ATV) with grade Ni-Co-Cr-Mo.

$$i(V) = [i_{o1} \cdot f_{BV}(V_1, B_1) + i_{P1}] \cdot \Sigma^{-}(V_a, \Delta_a) + [i_P + i_{o2} \cdot f_T(V_2, B_2) + i_{o3} \cdot f_T(V_3, B_3)] \cdot \Sigma^{+}(V_b, \Delta_b)$$

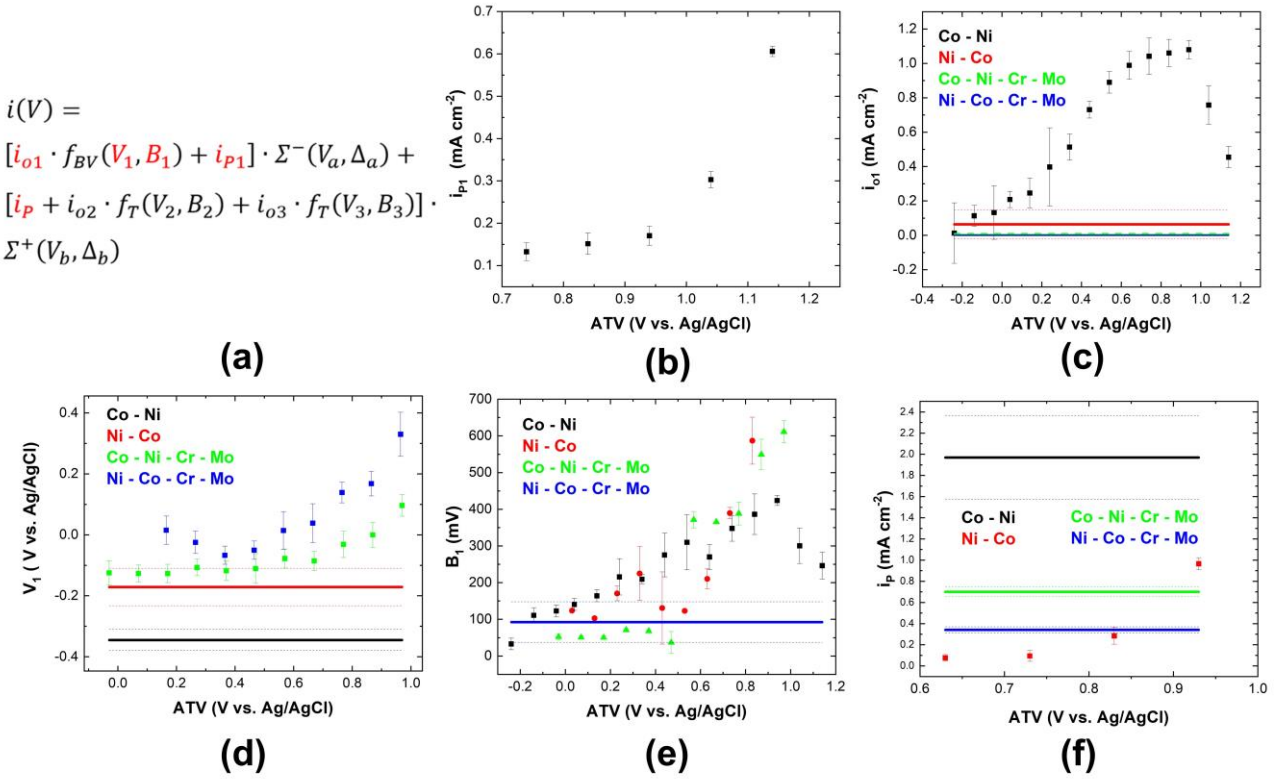


**Figure S6.** Fit parameters for Eq. (S1) (see also Panel (a)), as a function of the ATV. (b) $i_{P1}$ for grade Co-Ni; (c) $i_{o1}$; (d) $V_1$; (e) $B_1$; (f) $i_P$.

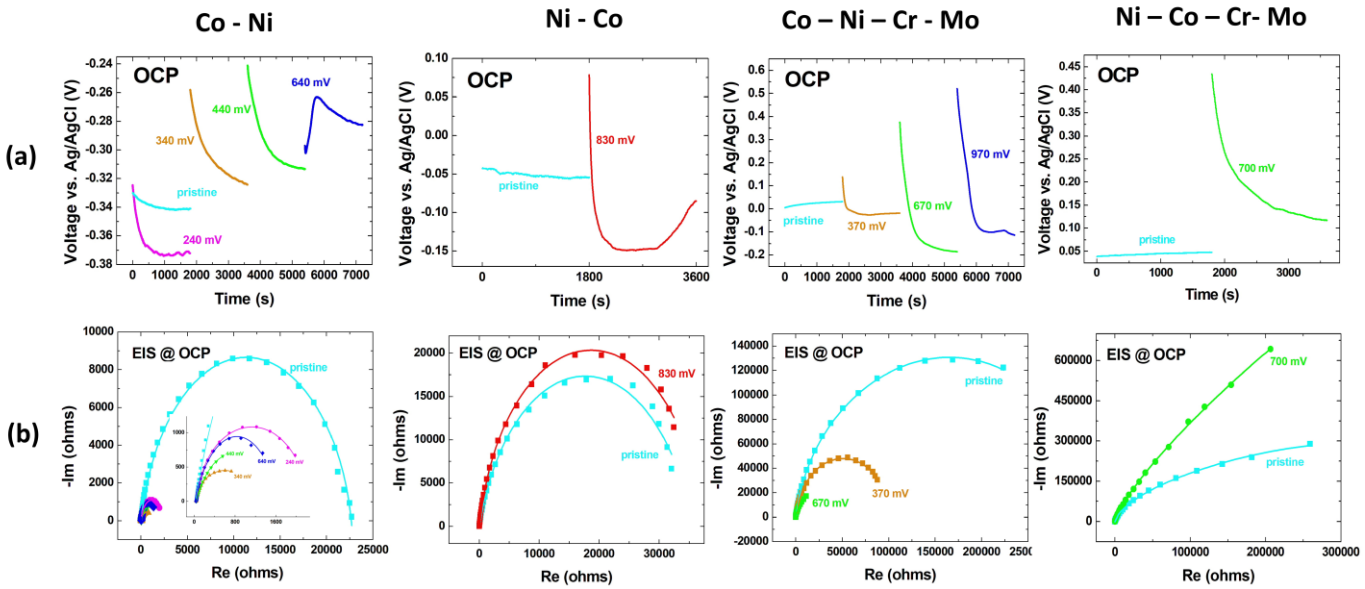


**Figure S7.** (a) OCP measurements carried out after the potentiostatic tests at the critical potentials $E_{crit}$ reported in Figure 3(a). (b) EIS spectra measured at OCP in pristine conditions and after the OCP relaxation of Panel (a).

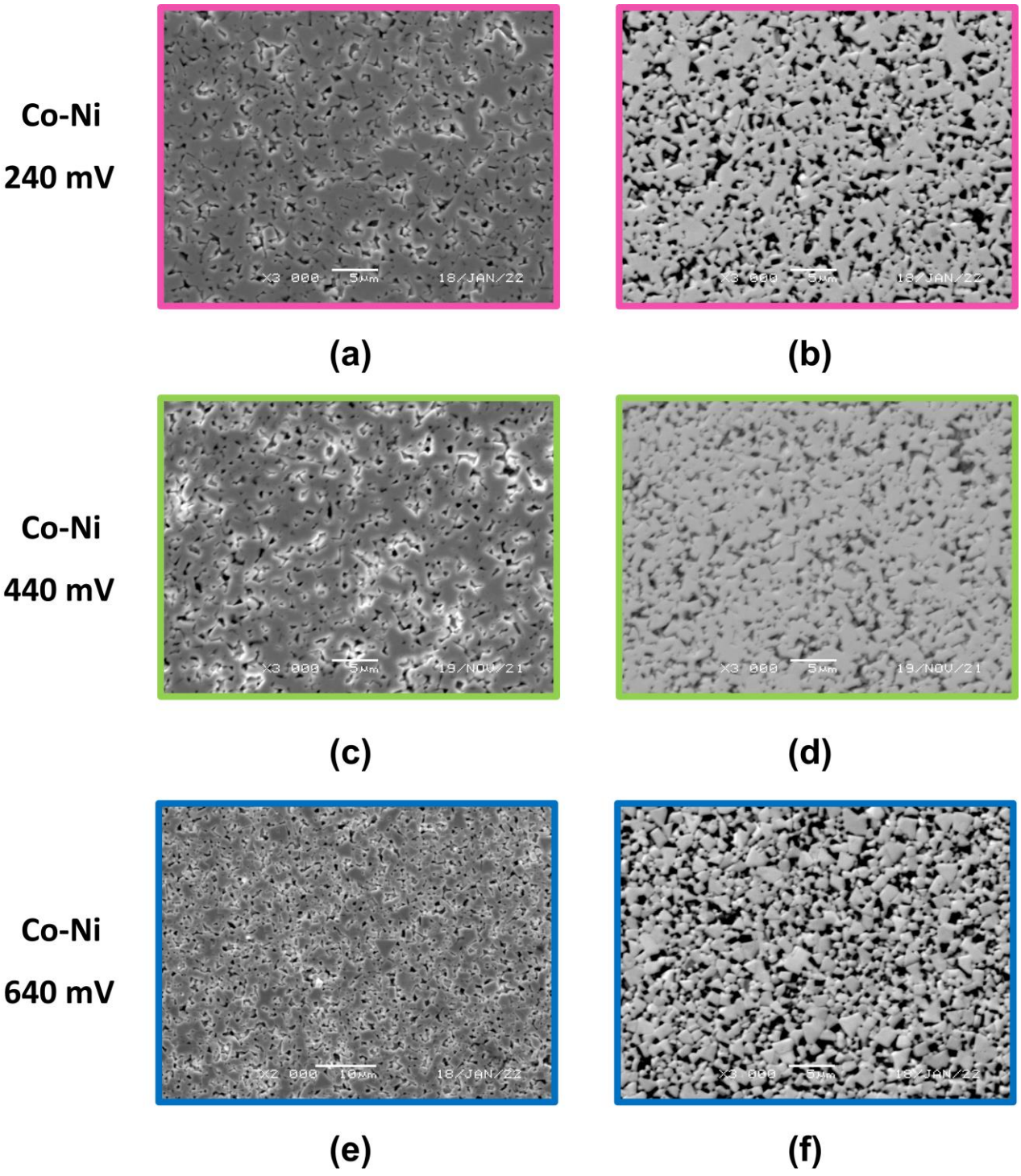


**Figure S8.** SEM micrographs of HM grade Co-Ni after potentiostatic polarization at the indicated potentials. Left column: secondary electron images; right column: backscattered electron images.

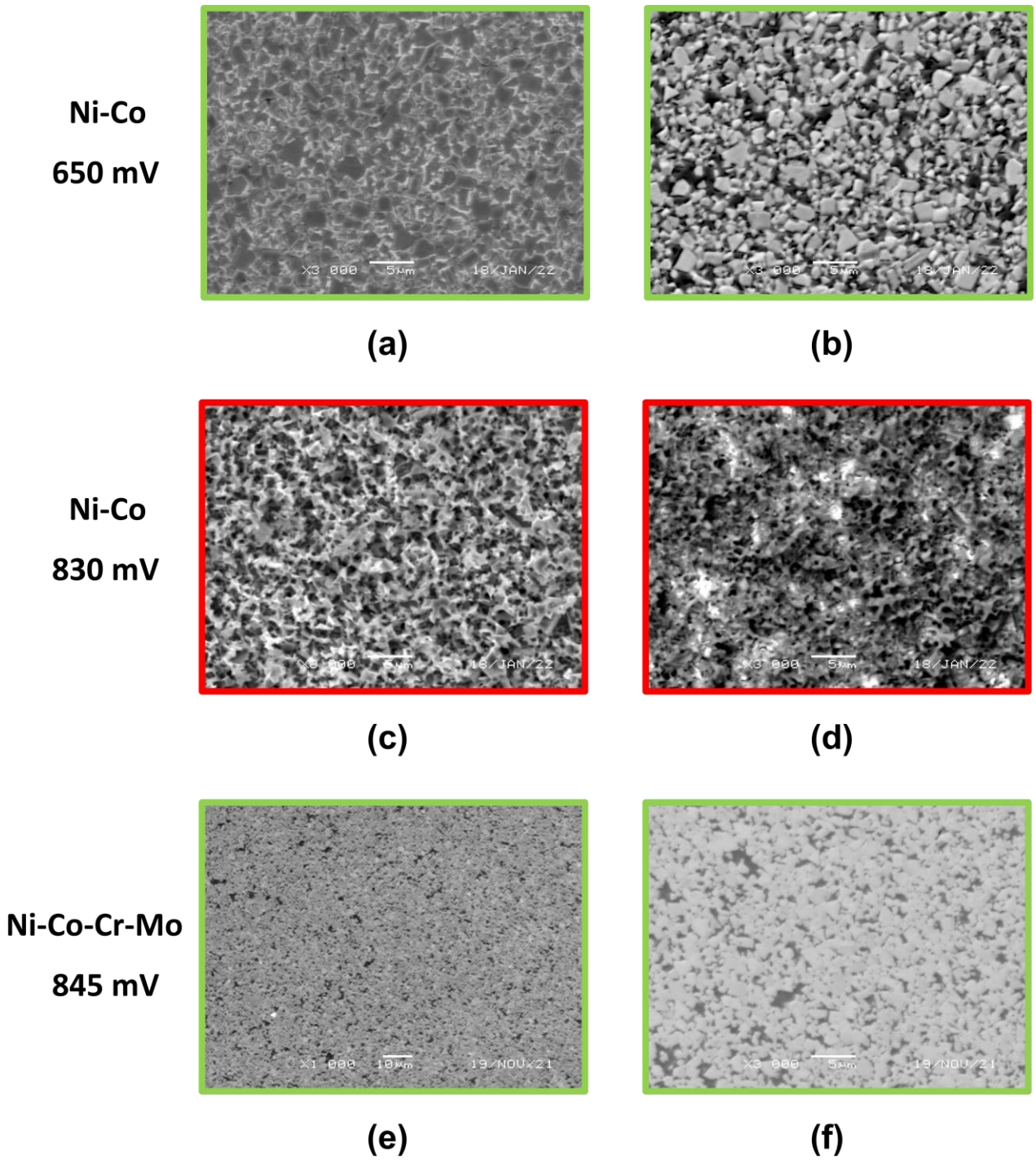


**Figure S9.** SEM micrographs of HM grades Ni-Co and Ni-Co-Cr-Mo after potentiostatic polarization at the indicated potentials. Left column: secondary electron images; right column: backscattered electron images.

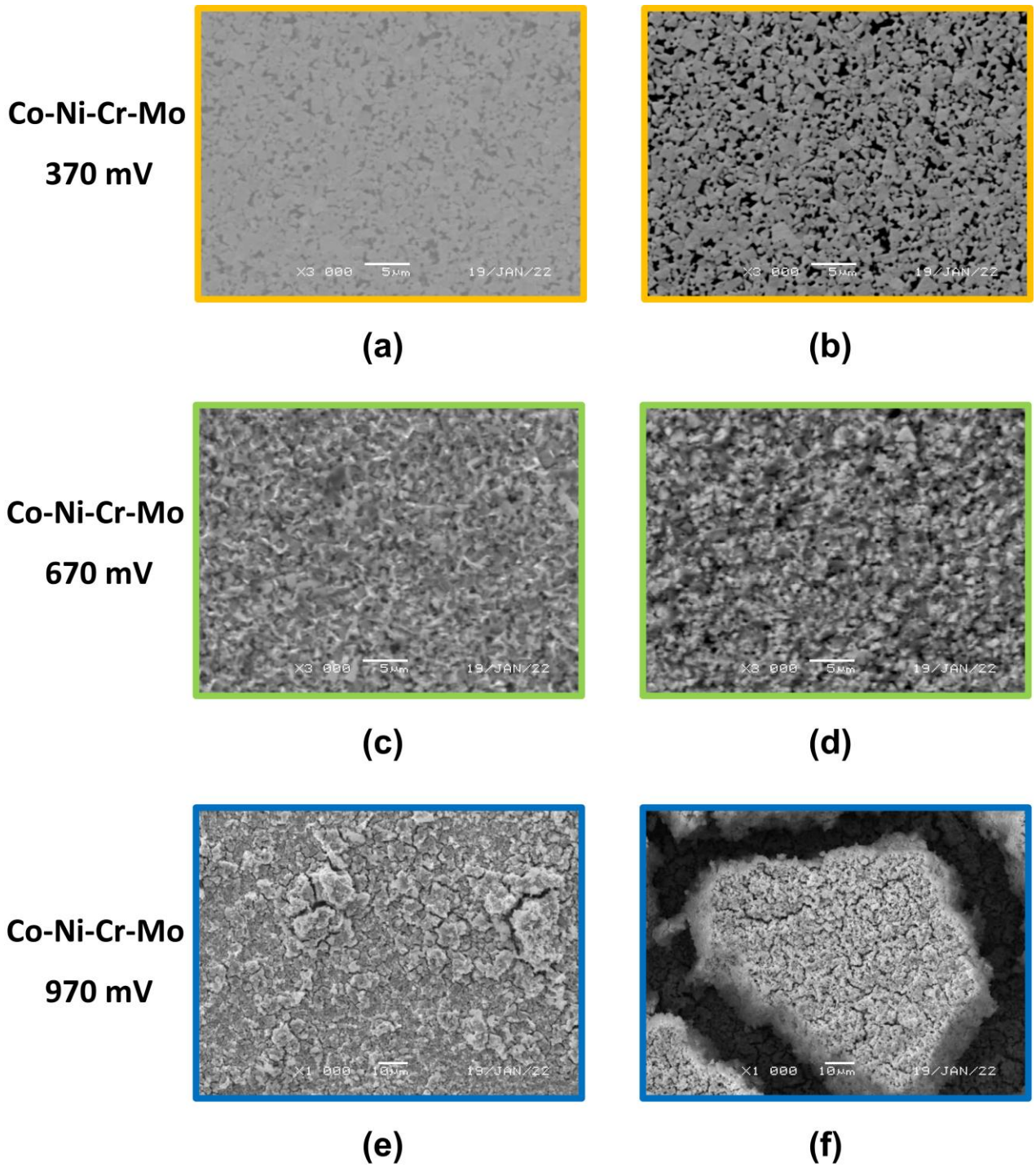


**Figure S10.** SEM micrographs of HM grade Co-Ni-Cr-Mo after potentiostatic polarization at the indicated potentials. Left column: secondary electron images; right column: backscattered electron images.

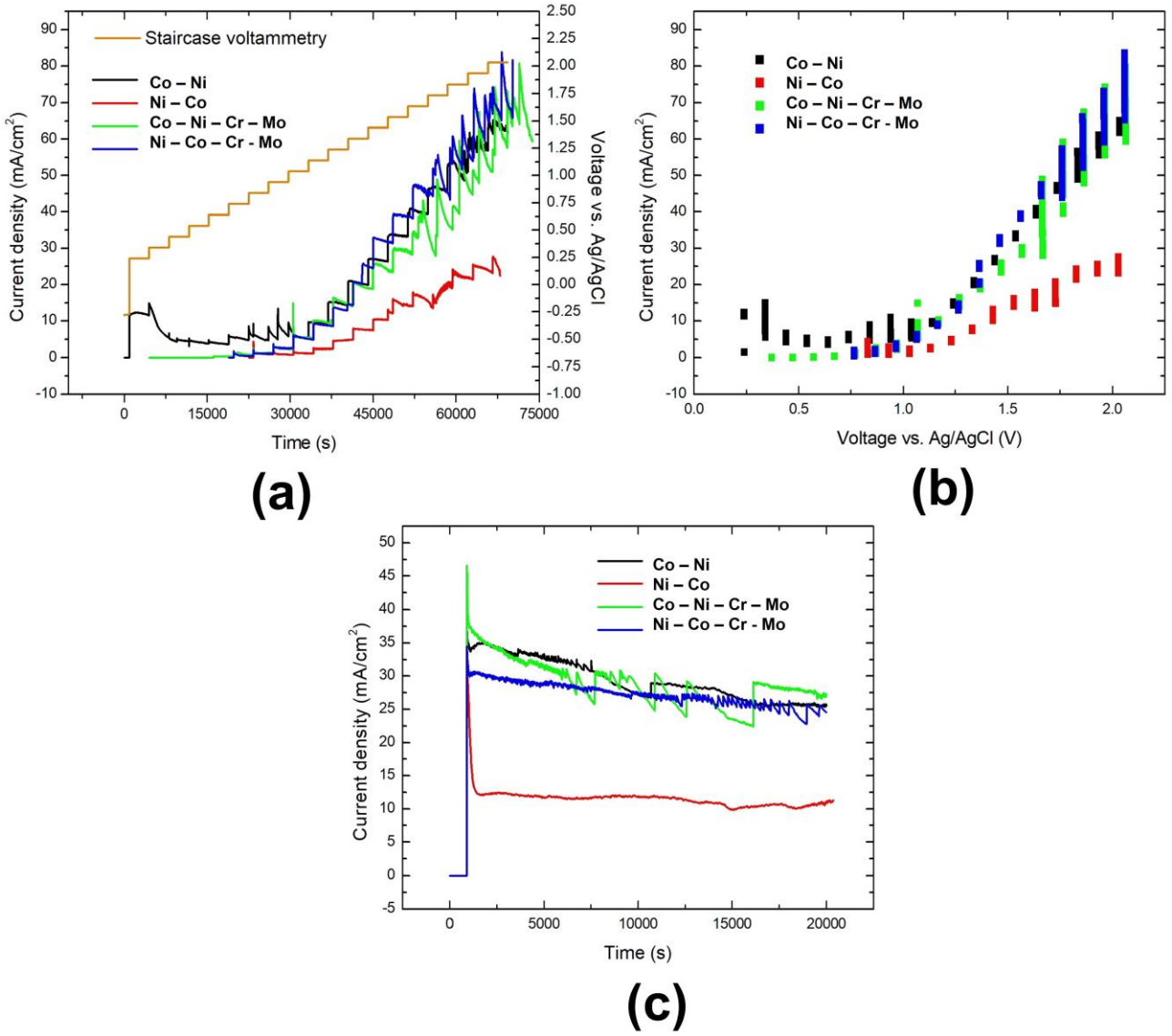


**Figure S11.** Anodic potentiostatic experiments extending into the OER region for the indicated HM grades. (a) Current density (c.d.) vs. time; (b) c.d. vs. applied potential; (c) chronoamperograms at 1.55 $V_{Ag/AgCl}$. Serration of the c.d. time-series at potentials in excess of 1.55 $V_{Ag/AgCl}$ denotes $O_2$ bubble formation and release.

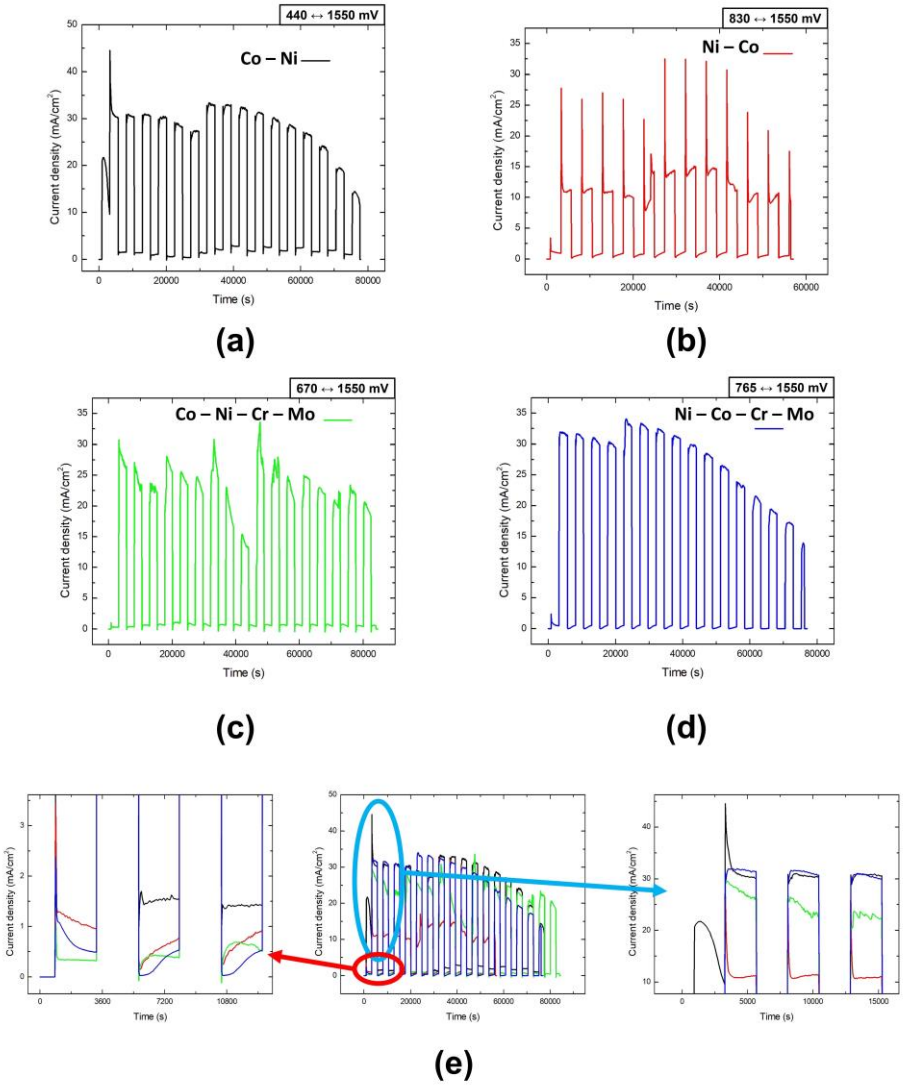


**Figure S12.** The c.d. time-series resulting from potentiostatic anodic square-wave cycling, leading to electrochemical HM demolition, for the four investigated grades: (a) grade Co-Ni; (b) grade Ni-Co; (c) grade Co-Ni-Cr-Mo; (d) grade Ni-Co-Cr-Mo. The low- and high-anodic potentials, specified in the images, are applied for 40 min each. Panel (e) compares the four time-series and shows details of the c.d. response to low- and high-anodic potentials.

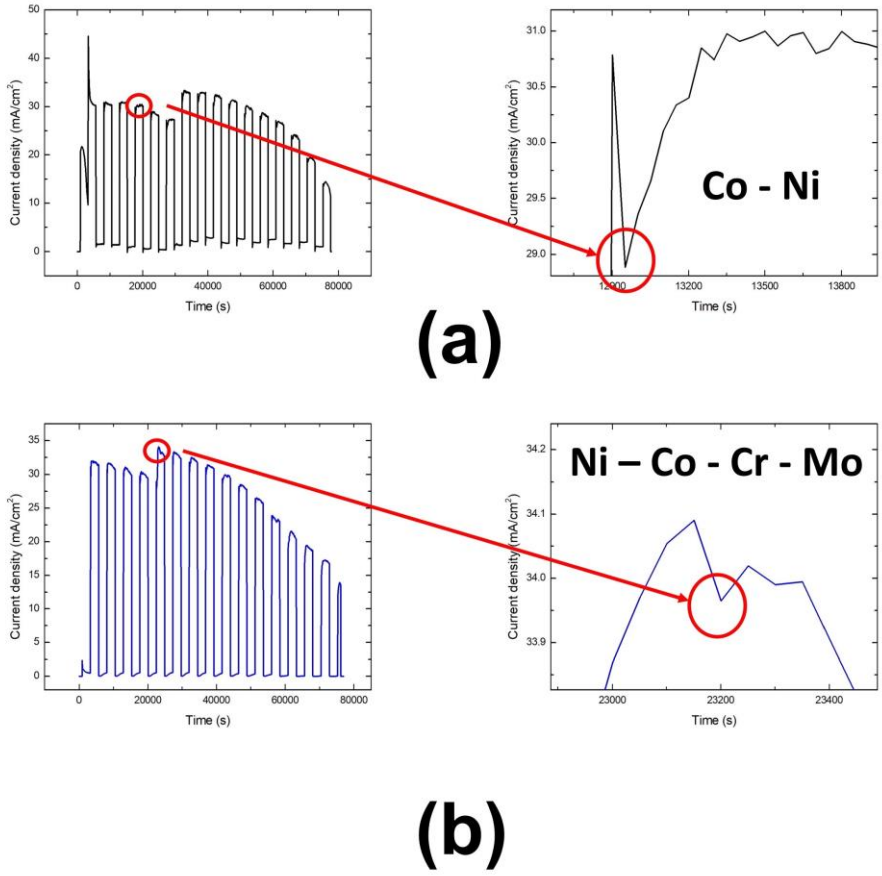


**Figure S13.** Details of the c.d. time-series resulting from pulsed anodic potentiostatic polarization for electrochemical HM demolition of grades Co-Ni (a) and Ni-Co-Cr-Mo (b), highlighting the electrochemical signature corresponding to the detachment of a corrosion product disk at each cycle.

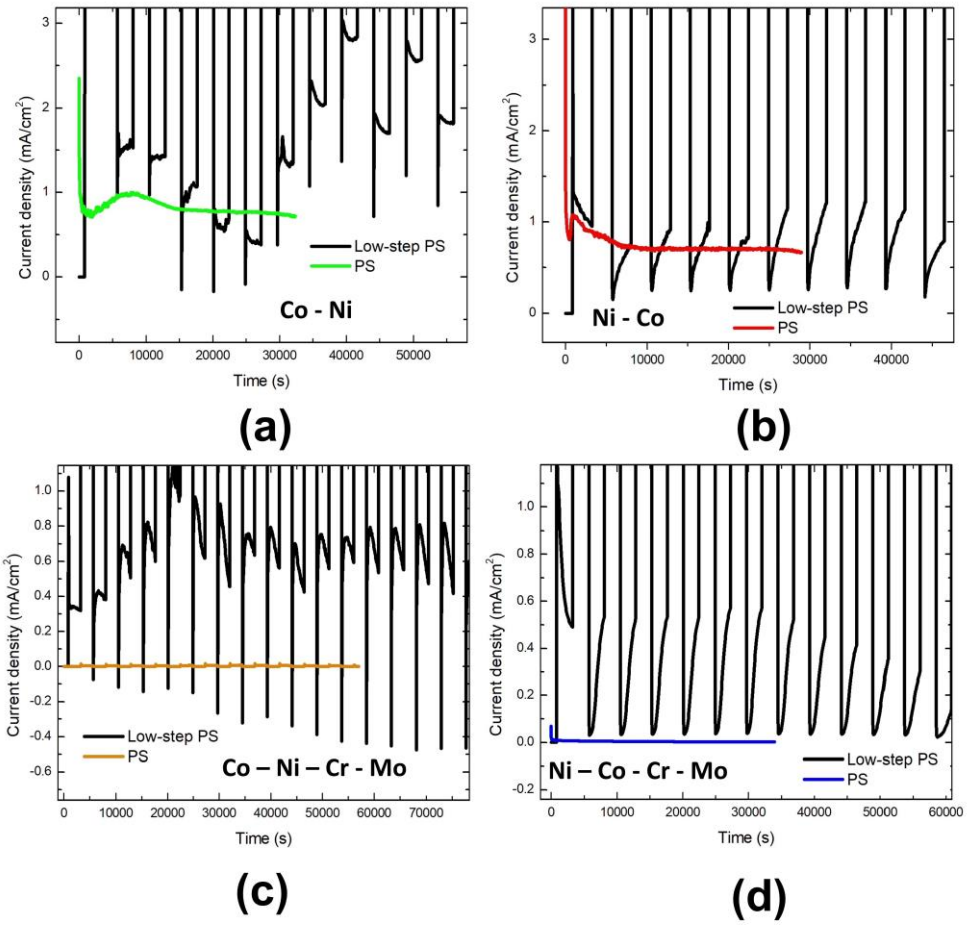


**Figure S14.** Comparison of the c.d. values corresponding to potentiostatic polarization in the low-anodic range: potential cycling (black lines) and constant potential (plotted in color) experiments for the HM grades are indicated.

**Table S1.** NLLS estimates and their 95% confidence levels for the model parameters of Eq.s (S1)–(S4).

| Grade | Co-Ni | Ni-Co | Co-Ni-Cr-Mo | Ni-Co-Cr-Mo |
|---|---|---|---|---|
| $i_{o1}$ ($mAcm^{-2}$) | see Fig. S6(c) | 0.0640±0.0830 | 0.0049±0.0053 | 0,0002±0,0003 |
| $V_1$ ($V_{Ag/AgCl}$) | -0.3450±0.0348 | -0.1714±0.0614 | see Fig. S6(d) | see Fig. S6(d) |
| $B_1$ (mV) | see Fig. S6(e) | see Fig. S6(e) | see Fig. S6(e) | 92.57±55.25 |
| A ($V^{-1}$) | 4.431E-3±5.182E-3 | 1.103E-4±1.489E-4 | N/A | N/A |
| $i_{P1}$ ($mAcm^{-2}$) | see Fig. S6(b) | N/A | N/A | N/A |
| $V_a$ ($V_{Ag/AgCl}$) | 0.3214±0.0140 | N/A | N/A | N/A |
| $\Delta_a$ (mV) | 27.91±18.28 | N/A | N/A | N/A |
| $i_P$ ($mA\ cm^{-2}$) | 1.9693±0.3976 | see Fig. S6(b) | 0.7008±0.0443 | 0.3416±0.0286 |
| $i_{o2}$ ($mA\ cm^{-2}$) | 0.4141±0.3975 | 0.0138±0.0072 | 0.0033±0.0032 | 0.0016±0.0013 |

| | | | | |
|---|---|---|---|---|
| $V_2$ (V) | 0.7035±0.0257 | 0.7043±0.0472 | 0.7285±0.0701 | 0.7898±0.0104 |
| $B_2$ (mV) | 209.6±96.8 | 67.22±1.85 | 62.87±11.18 | 74.23±19.65 |
| $i_{o3}$ (mA $cm^{-2}$) | 0.0163±0.0031 | 0.0158±0.0078 | 0.0097±0.0039 | 0.0029±0.0011 |
| $V_3$ (V) | 0.6538±0.0421 | 0.6800±0.0960 | 0.6536±0.0399 | 0.6934±0.0532 |
| $B_3$ (mV) | 418.7±210.4 | 162.4±33.6 | 161.0±002.5 | 96.04±3.42 |
| $V_b$ ($V_{Ag/AgCl}$) | 0.7080±0.0195 | 0.7908±0.0215 | 0.7607± 0.0874 | 0.8241± 0.011 |
| $\Delta_b$ (mV) | 46.27±19.30 | 50.36±48.71 | 61.95± 30.71 | 27.52±31.18 |